

ALTERATION OF THE GRAPHITE MORPHOLOGY IN SOLID SOLUTION-STRENGTHENED DUCTILE IRON DUE TO HIGH CONTENTS OF CERIUM AND BISMUTH

Felix Stieler and Babette Tonn 

Institute of Metallurgy, Clausthal University of Technology, Robert-Koch-Str. 42, 38678 Clausthal-Zellerfeld, Germany

Daniel Funk

Georg Funk Eisengießerei GmbH & Co. KG, Turnstr. 39, 73430 Aalen, Germany

Copyright © 2022 The Author(s)
<https://doi.org/10.1007/s40962-022-00857-y>

Abstract

The impact of combined addition of high levels of bismuth up to 120 wt ppm and cerium up to 2000 wt ppm on the graphite morphology in GJS 450-18 with 3.2 wt% carbon and 3.2 wt% silicon was studied. Experiments were conducted with insulated keel blocks with a solidification time of 40 min. Samples from the thermal centre of the castings were analysed by optical microscopy, and the forms and sizes of graphite particles were characterised. Bismuth addition, even at 25 wt ppm, resulted in an altered graphite form in the last-to-freeze regions resembling intercellular lamellar graphite (ILG). Additions of 45 wt ppm or more Ce to these Bi-containing melts prevented the formation of ILG and produced chunky graphite (CHG) instead. ILG did not appear for ratios Bi/Ce > 1.5, while CHG could not be found for ratios Bi/Ce < 0.7. Only one type of graphite degeneration (either ILG or CHG) was

present in each sample, thus rendering their formation mutually exclusive. Larger amounts of Ce between 300 and 500 wt ppm resulted in the formation of predominantly graphite form V, while no degenerations could be observed. The addition of Ce to a Bi-contaminated cast iron melt to avoid ILG formation and achieve a regular graphite structure with mainly form VI graphite is not possible. Instead, form V replaces form VI as the predominantly formed morphology. Ce levels higher than 1000 wt ppm resulted in the formation of large areas of undercooled graphite in the last-to-freeze regions regardless of the Bi content in the cast iron melt.

Keywords: ductile cast iron, graphite morphology, interfering elements, antimony, cerium, chunky graphite

Introduction

The mechanical properties of ductile cast iron (DI) are determined by the iron matrix as well as by the amount of graphite and its morphology. To increase the tensile strength of unalloyed DI, which usually has a ferritic matrix, pearlite-promoting elements like copper will be added to the melt. This is accompanied by a severe loss of ductility. As an alternative to pearlitisation, the strength of the ferrite can be increased by alloying with elements dissolved in the solid solution, thus producing a solution-strengthened cast iron (SSDI). In this way, strengths comparable to pearlitic microstructures can be achieved

while maintaining the much higher ductility of ferrite.¹⁻³ The yield strength ratio of ferritic DI is higher compared with pearlitic DI as well.^{1,3}

The mechanical properties of the matrix are negatively impacted by graphite present in the microstructure and in particular by unfavourable morphologies. Besides standardised graphite forms from lamellar (form I) over vermicular (form III) to nodular graphite (form V and VI) according to ISO 945 1, degenerated graphite forms may occur in DI as well.⁴⁻⁷ These degenerations can be divided into two groups, which differ in terms of morphology, time of formation during solidification and causative elements. In the first group are chunky graphite (CHG) and exploded graphite (EG) whereby EG is an intermediate between regular nodular graphite and CHG.^{7,8} Intercellular lamellar

graphite (ILG) constitutes the second group under which the not clearly differentiable forms spiky, crab and mesh graphite are summarised.^{9–13}

The occurrence of graphite degeneracy is caused by long solidification times and elevated concentrations of certain elements. The critical concentrations of elements above which graphite degeneracy occurs depend on the solidification time, and the concentration limit decreases with longer solidification times.^{13–19} Regarding graphite morphology, these elements are hence called interfering elements and can be divided into two groups, according to the degenerated morphology they cause. Verified chunky graphite promoters are Al, Ca, Ce, Ni and Si, while ILG is promoted by the elements As, B, Bi, Cu, Pb, Sb and Sn.^{10,11,20–22} Most interfering elements are not commonly alloyed in cast iron and are likely to be present only in minute quantities.

Silicon is used to avoid carbide formation during solidification in all grey and ductile cast irons. However, in SSDI it is used in higher amounts up to 4.2 wt% to increase the strength of the material. SSDI is therefore much more susceptible to CHG formation compared with regular DIs that have lower Si contents.^{14,17,20,23} As the effect of the interfering elements on the graphite form is cumulative, the critical concentrations of other elements than Si are reduced and can reach unrealistically low values.^{6,14,17} Thus, the thickness of castings that can be produced in SSDI without degenerated graphite is limited, as the silicon content itself can become the constraining factor.^{14,17,23}

The presence of elements from only one group usually has a much more detrimental effect on the graphite morphology compared with intermediate contents of elements from both groups due to chemical reactions and intermetallic phase formation between members of the two groups.^{15–17,23,24} Bi and Ce already exert a major influence on the morphology of graphite at low concentrations, even compared with other interfering elements.^{21,25–27} Hence, their admissible concentrations are in a low ppm range.²⁷

Cerium is commonly used as an alternative nodularising agent to magnesium in concentrations up to 500 ppm by weight in thin-walled castings. Furthermore, it is a low-concentration ingredient in some inoculants and nodularisers as it can increase nodule density¹⁰ and avoid graphite degenerations that are caused by minute amounts of elements from the ILG group.^{10,11,28,29} The CHG promoters Ce, Ca and Al are very reactive and can hence be removed from the melt by oxidation. As elements in the ILG group are lower in reactivity, they cannot be removed from the melt as easily. However, elements from the chunky graphite group have been shown to lessen the effect of elements from the ILG group and vice-versa.^{15,17,24} Thus, low levels of cerium allow for the use of lower grade metallic scraps as it can counteract the trace amounts of

ILG-promoting elements. Ce does, however, inevitably increase the risk of formation of chunky graphite.^{16,17,20,24,26}

Bismuth is used in inoculating agents, as its intermetallic compounds are effective nucleation sites for graphite and the nucleating effect fades very slowly.^{11,30} However, the formation of graphite degeneration has been observed already at contents of 30 wt ppm Bi.³¹ Like Ce, it is used to prevent graphite degenerations by elements from the opposing group, hence preventing CHG formation.^{10,28,29} In thick-walled castings with a thermal module of 6.5 cm and prone to CHG formation, 20 wt ppm Bi added to the cast iron melt during inoculation has been shown to effectively prevent CHG formation and provide good graphite refinement.³⁰

Several papers have been written about the interaction of elements promoting ILG and CHG in general and for Bi and Ce specifically. The intermetallic compounds Ce_3Bi_4 and $CeBi$ precipitate in the liquid phase of cast iron at melt temperatures far surpassing those of usual cast iron processes.^{32,33} Thus, one of the elements can be used to counteract graphite degeneration caused by the other element. This interaction has been repeatedly described for widely varying compositions of cast iron as well as for different levels and ratios of Bi and Ce.^{10,28–30} However, the results on the influence and interaction of graphite degenerating elements in conventional DIs can be hardly extrapolated to SSDIs due to their inherently greater tendency to form graphite degenerations. To increase the potential of SSDI for use in castings with larger cross sections, we want to investigate the ability of Bi to prevent CHG formation in these irons. Here, Ce will be added in ascending amounts and combined with different amounts of Bi. This will allow the assessment of the interaction of Ce with Bi and its effects on the graphite morphology in SSDI over a wide composition range.

Experiments

A series of 24 cast iron keel blocks with a thickness of 75 mm below the feeder (geometry Y-IV taken from ISO 1083³⁴) and a weight of 25 kg each were cast with varying Ce and Bi contents. The cast iron was produced in four batches of 160 kg each with 3.2 wt% C and 3.2 wt% Si. Armco iron and pig iron were melted in a medium-frequency coreless induction furnace, and the composition was adjusted with graphite and ferrosilicon. The cast iron was tapped at a temperature of 1500 °C into a ladle preheated to 950 °C and treated with a FeSiMg master alloy containing 5.6 wt% Mg. Alloying Bi by having it sit in the mould and then be dissolved by the iron flowing in from below proved to be unsuccessful in the first run of experiments for specimen 1 to 6 as can be seen by their miniscule concentration of Bi given in Table 1. This method

Table 1. Final Composition of All Specimens, Ce and Bi Contents Measured by ICP-OES

Sample	Bi (wt ppm)	Ce (wt ppm)	Ce/Bi	C (wt%)	Si (wt%)	Mn (wt%)	P (wt%)	S (wt%)	Mg (wt ppm)
1	2	195	97.5	3.28	3.18	0.02	0.01	0.007	390
2	2	159	79.5	3.28	3.18	0.02	0.01	0.007	390
3	5	155	31	3.28	3.18	0.02	0.01	0.007	390
4	5	1430	286	3.28	3.18	0.02	0.01	0.007	390
5	5	1720	344	3.28	3.18	0.02	0.01	0.007	390
6	2	1630	815	3.28	3.18	0.02	0.01	0.007	390
19	25	< 10	< 0.4	3.14	3.31	0.06	0.02	0.011	310
20	24	36	1.5	3.14	3.31	0.06	0.02	0.011	310
21	25	78	3.12	3.14	3.31	0.06	0.02	0.011	310
22	31	169	5.5	3.14	3.31	0.06	0.02	0.011	310
23	24	370	15.4	3.14	3.31	0.06	0.02	0.011	310
24	25	774	31.0	3.14	3.31	0.06	0.02	0.011	310
7	73	< 10	< 0.14	3.1	3.34	0.02	0.01	0.008	350
8	64	44	0.69	3.1	3.34	0.02	0.01	0.008	350
9	64	100	1.56	3.1	3.34	0.02	0.01	0.008	350
10	76	339	4.46	3.1	3.34	0.02	0.01	0.008	350
11	79	594	7.5	3.1	3.34	0.02	0.01	0.008	350
12	78	1117	14.3	3.1	3.34	0.02	0.01	0.008	350
13	110	< 10	< 0.09	2.98	3.1	0.05	0.01	0.012	300
14	114	37	0.32	2.98	3.1	0.05	0.01	0.012	300
15	116	217	1.87	2.98	3.1	0.05	0.01	0.012	300
16	114	236	2.07	2.98	3.1	0.05	0.01	0.012	300
17	119	627	5.3	2.98	3.1	0.05	0.01	0.012	300
18	124	2040	16.5	2.98	3.1	0.05	0.01	0.012	300

worked for the pure Ce employed and yields of around 50% could be achieved, although the yield varied a lot. In the following runs, pure Bi was added together with the Mg-containing master alloy and a yield of approximately 60% could be achieved for Bi. The melt was then inoculated with 0.2 wt% of a FeSi75 inoculant containing 2 wt%

of Ba. At this point, a sample was taken for the determination of final composition by spark-OES.

The mould consisted of furan resin-bound quartz sand. Six keel blocks were connected by a joint gating system, as shown in Figure 1a. They were completely enveloped with

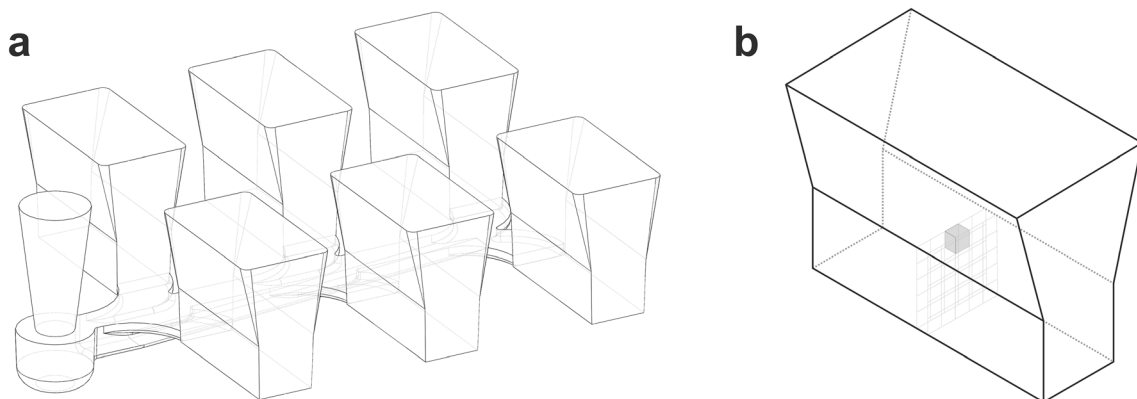


Figure 1. (a) Model of keel blocks with casting system, (b) sample (grey block) taken from the keel block for microstructure investigations.

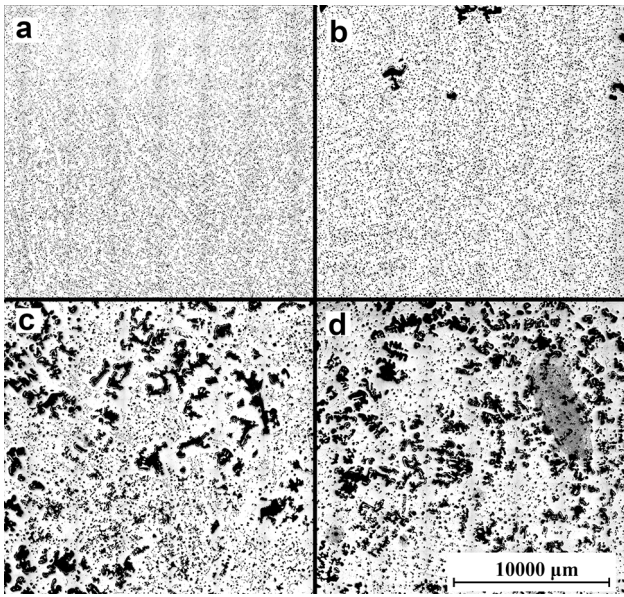


Figure 2. Microstructures with different fractions of porosity increasing with the amount of Ce: (a) sample 8 (Ce = 44 wt ppm), (b) sample 9 (Ce = 100 wt ppm), (c) sample 10 (Ce = 339 wt ppm), (d) sample 11 (Ce = 594 wt ppm).

20-mm plates of insulating porous alumina fibre which increased the solidification time to 40 min. Pure Ce was alloyed separately in each sample cavity at different concentrations by placing an appropriate amount of wire cuttings in it. Upon contact with the iron, the Ce melted and mixed with the liquid iron. Thus, six different Ce contents could be investigated for each level of Bi.

Specimens for metallography were then taken from the thermal centre of the castings, which is located close to the

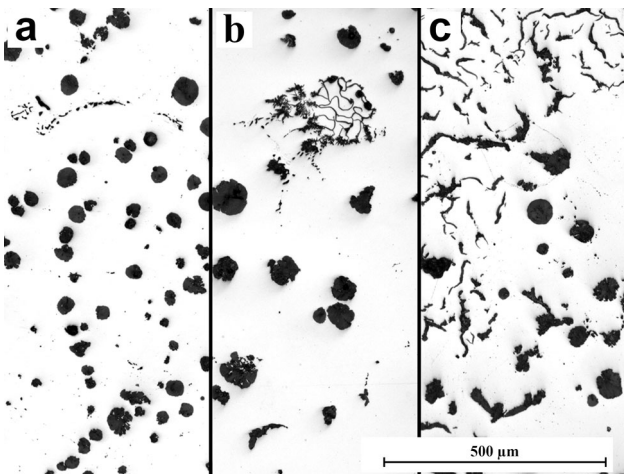


Figure 3. Evolution of intercellular graphite from (a) 25 wt ppm Bi (specimen 19) over (b) 73 wt ppm Bi (specimen 7) to (c) lamellae at 110 wt ppm Bi (specimen 13).

feeder, as shown in Figure 1b. This area has the longest solidification time in the casting and thus the highest probability of graphite degeneration. Each sample was ground and polished, and a graphite analysis according to ISO 945 1, 2 and 4^{4,5,35} was performed with 10 micrographs at 100× magnification each. Areas with degenerated graphite were manually marked as described in,²⁶ and that area was counted as degenerated. These marked areas were excluded from the pictures for further automated analysis of graphite particles. Thereby, the changes to the regular graphite could be analysed besides the amount of degenerated graphite formed. For better visualisation, the results of the graphite particle analysis were mathematically modelled using partial least squares regression.

Results

The chemical compositions of the melts were determined by spark-OES and are given in Table 1. The concentrations of Ce and Bi were measured by ICP-OES for each specimen individually as Ce was alloyed separately and might have reacted with Bi, changing the amount in solution. To attain the composition for the exact place where the microstructure was investigated, chips for ICP-OES were produced from the backside of metallography specimens.

The keel block geometry was chosen because of its excellent feeding capability. However, increasing Ce contents cause higher amounts of shrinkage porosity inside the castings, as shown in Figure 2. Here, samples were chosen from the same melt but with different Ce contents. Thus, other metallurgical or chemical influences of the melt on porosity can be neglected. In sample 11, which has a Ce content of 594 wt ppm, even macroscopic shrinkage as

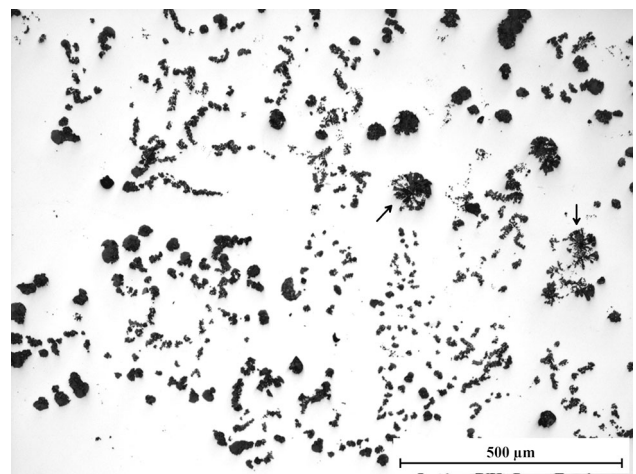


Figure 4. Microstructure of sample 16 consisting of large areas of CHG, regular graphite and some EG particles (marked by arrows).

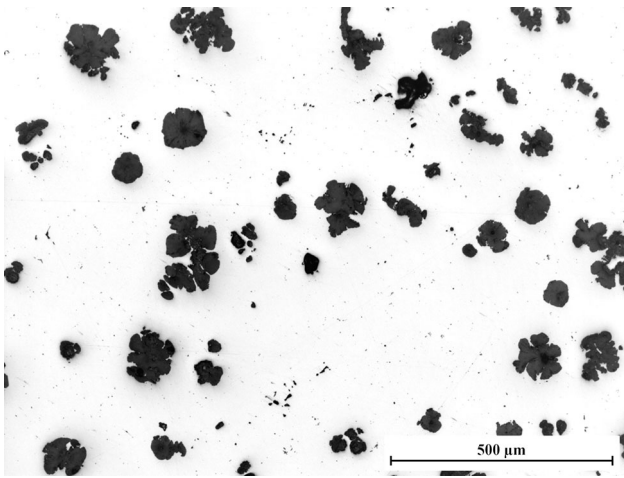


Figure 5. Microstructure of sample 24 (774 wt ppm Ce) showing mainly form V graphite. The smallest dark particles are microporosities and may not be mistaken for graphite.

well as sink marks on the surface of the castings could be observed.

The precipitated graphite presented itself in varying forms depending on the amounts of interfering elements. ILG was found in samples 7, 13, 14, 19 and 20. While the form of the degenerations evolved with rising content of Bi, they are always located in the LTF regions, shown in Figure 3. As the amount of ILG increases with rising Bi concentration, it eventually occupies large areas of the microstructure. An identification of the LTF area by the graphite structure is no longer possible at that point. Graphite particles classifiable as ILG could not be found in samples that contained more than 37 wt ppm of cerium.

ILG was found even at around 25 wt ppm Bi as depicted in Figure 3a, though the presented morphology is less dramatic compared with those found higher levels of Bi. Fully formed ILG as in Figure 3b appeared at 73 wt ppm Bi. The very high amounts of Bi above 100 wt ppm resulted in growth of graphite with forms I, II and III as shown in Figure 3c. ILG occurred up to ratios of Ce/Bi = 1.5 (specimen 20).

CHG was present in samples containing between 44 wt ppm Ce (sample 8 with 64 wt ppm Bi) and 370 wt ppm Ce (sample 23 with 24 wt ppm Bi). Particles were characterised as CHG when they had a form reminiscent of corals, were notably smaller compared with regular nodules, had shorter distances to the nearest neighbour and were not located in the LTF regions. From deep-etched samples and computer tomography, it is known that CHG consists of an interconnected network of graphite particles.²⁶ A well-formed example of a region with CHG is shown in Figure 4 from sample 16, which contained 42% CHG by area.

Exploded graphite (EG) was always present besides the CHG. Drawing a line between both morphologies is difficult, as the spaces between the sub-particles in exploded graphite increase until it would be considered CHG. Therefore, EG area was counted together with CHG. Two exemplary EG particles can be seen in the middle and to the right in Figure 4, marked by arrows.

For concentrations of Ce between 78 wt ppm Ce (sample 21) and 774 wt ppm (sample 24), no degenerated graphite could be found in some samples (9, 10, 17, 21, 24). The microstructure of sample 24 is shown in Figure 5 and is exemplary for samples 9, 10, 17, 21 and 24. Here, mainly very large form V graphite particles precipitated. As these

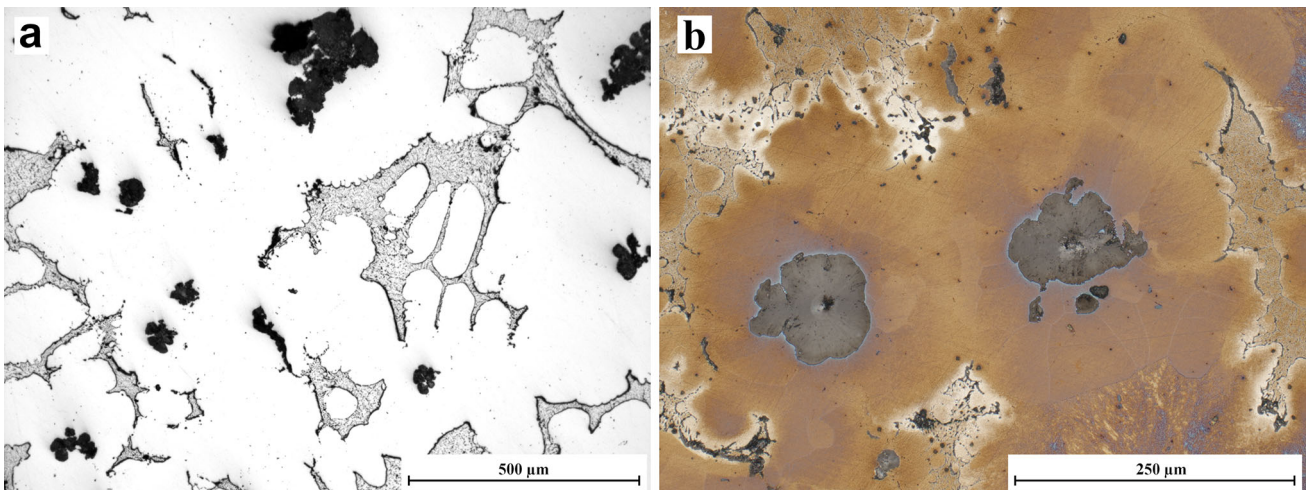


Figure 6. Microstructure at very high Ce content in sample 6 (1630 wt ppm Ce) (a) UG in the LTF regions, (b) picric acid etching (LePera) showing Si segregation in the iron matrix from graphite sphere (blue, high Si content) to UG (white, lowest Si content).

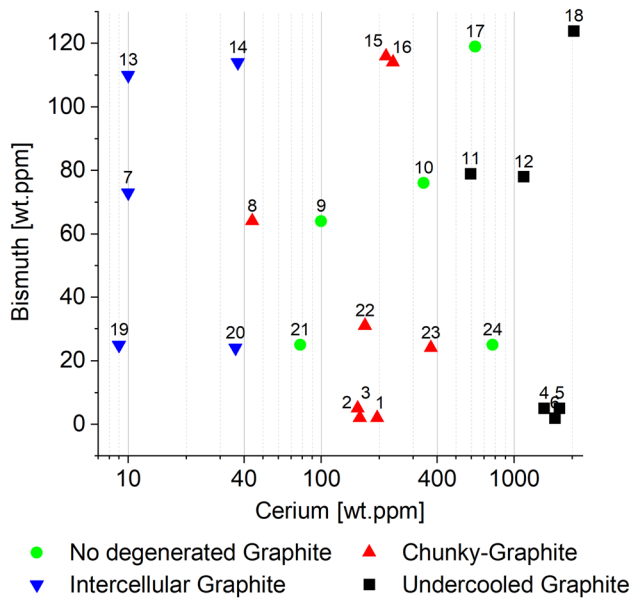


Figure 7. Occurrence of graphite degenerations at different concentrations of Ce and Bi.

samples have high amounts of Ce, microporosity is apparent between individual grains.

For even higher levels of Ce, large areas of extremely fine structured graphite in the LTF areas could be observed as shown in Figure 6a for sample 6 with 1630 wt ppm Ce. The individual graphite particles in the cross section are so small that a preferred growth direction could not be discerned. Formation of this morphology reminiscent of undercooled graphite (UG) or “D-graphite”⁴ started at 594 wt ppm in sample 11 and happened in all samples surpassing 1000 wt ppm regardless of content of Bi or Ce/Bi ratio.

In Figure 6b, the segregation of the silicon is shown by etching with picric acid according to LePera. Bluish shades of the matrix visible around the graphite nodules indicate a high silicon content, while the matrix around the UG appears white, which indicates a lower Si content. As Si content decreases over the course of the solidification, this proves the late precipitation of the UG compared with the

Table 2. Graphite Characterisation from Optical Micrographs According to ISO 945 1, 2 and 4^{4,5,35} and Degenerations Quantified According to,²⁶ Samples Marked Bold Contained UG and were Excluded from Further Analysis

Sample	Bi (wt. ppm)	Ce (wt. ppm)	Ce/Bi	Particles (1/mm ²)	Nodularity	Graphite III (%)	Graphite V (%)	Graphite VI (%)	CHG area (%)	ILG area (%)	UG area (%)
1	2	195	97.5	51	61.7	7	53.8	36.9	3.1	–	–
2	2	159	79.5	83	64.5	5.9	58.1	35.3	13.9	–	–
3	5	155	31	95	42.6	32.1	47.9	20	28.9	–	–
4	5	1430	286	88	23.7	49.5	36.1	1.9	–	–	9.3
5	5	1720	344	164	17	51.6	30.4	0.5	–	–	19.7
6	2	1630	815	136	25	56.9	33.4	3	–	–	19.9
19	25	< 10	< 0.4	182	68.7	4.9	51.9	41.7	–	1.1	–
20	24	36	1.5	191	66.7	5	60.1	34	–	0.8	–
21	25	78	3.12	234	63.5	6.8	59.1	32.6	–	–	–
22	31	169	5.5	182	59.7	8.5	55.8	31.9	6.5	–	–
23	24	370	15.4	105	57.7	11	63.1	22.4	7.2	–	–
24	25	774	31.0	88	61.8	4.7	72.6	17.2	–	–	–
7	73	< 10	< 0.14	73	62.3	11.2	62.1	26.2	–	1.8	–
8	64	44	0.69	120	35.6	36.1	44.7	15.8	15.5	–	–
9	64	100	1.56	51	56.6	6.3	81.5	12.2	–	–	–
10	76	339	4.46	29	52.4	8.8	88.4	2.8	–	–	–
11	79	594	7.5	33	36.8	21.5	62.2	3	–	–	5
12	78	1117	14.3	59	25.7	55.3	38	3.3	–	–	7.1
13	110	< 10	< 0.09	136	29.3	64.7	16.2	19.1	–	21.9	–
14	114	37	0.32	90	54.9	16.6	56.3	26.8	–	1.4	–
15	116	217	1.87	184	37	38.6	43.5	16.7	25.8	–	–
16	114	236	2.07	191	34.6	38.4	46.5	14.1	42.1	–	–
17	119	627	5.3	43	41.2	29.9	59.4	6.7	–	–	–
18	124	2040	16.5	80	31.8	50.2	41.3	8.5	–	–	14

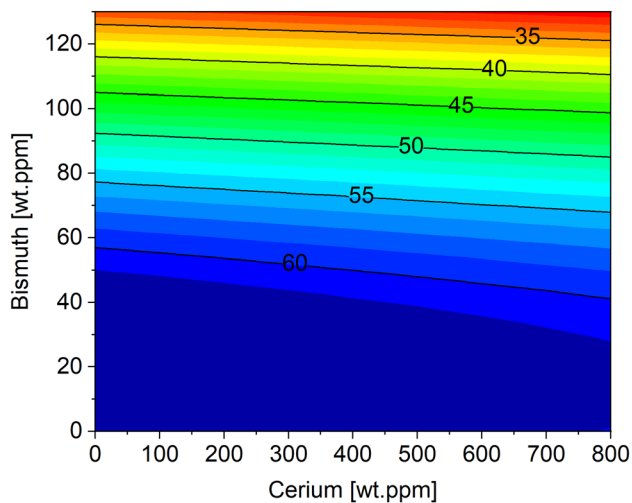


Figure 8. Modelled nodularity of the non-degenerated graphite particles.

graphite spheroids. The remaining graphite particles are mainly of form V.

Different degenerated graphite forms, especially CHG and ILG, were never present together in the same sample. Therefore, each sample has been characterised by the occurring degenerated graphite morphology, as shown in Figure 7. The Ce/Bi ratios and the concentration ranges of Ce and Bi of the samples without degenerates overlap with those of the samples with degenerations. Why degenerated graphite did not occur in certain samples as opposed to others is not immediately obvious.

The results of graphite particle analysis for each alloy are listed in Table 2. Degenerated graphite particles were excluded, and only regular graphite particles were used to calculate particle density, nodularity and the fractions of forms III, V and VI. To improve the interpretability of the results, they have been mathematically modelled by partial least squares regression. The isolated data points are thereby transformed into plottable functions, graphically represented in Figures 8, 9, 10, 11, 12 and 13. Graphite particle density could not be modelled with sufficient quality (R^2 and $Q^2 > 0.6$) and was therefore not further investigated. All CHG, ILG and UG particles were excluded before graphite parameter determination. Thus, the mathematical models can only represent the changes in the morphology of regular graphite.

For the modelling of graphite parameters, specimens with undercooled graphite (4, 5, 6, 12 and 18) were excluded. Their very high Ce contents of more than 1000 wt ppm compared with the other Ce contents up to around 600 wt ppm and only sample 24 with 774 wt ppm in between represent a large gap in the data distribution which has a negative impact on the model prediction accuracy.

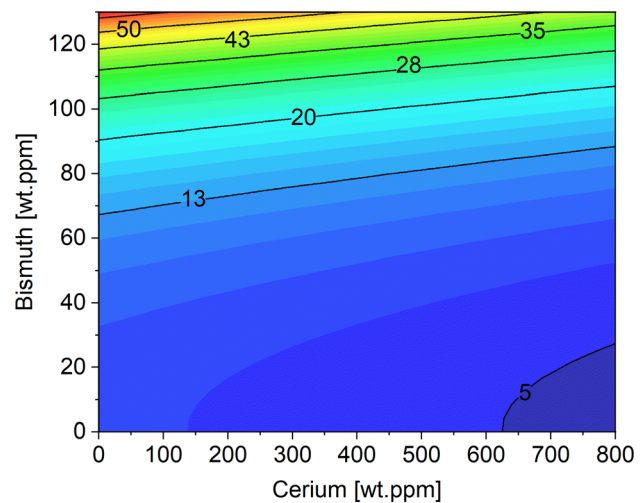


Figure 9. Modelled proportion of the graphite particles with form III on the total number of graphite particles depending on the amount of Ce and Bi present.

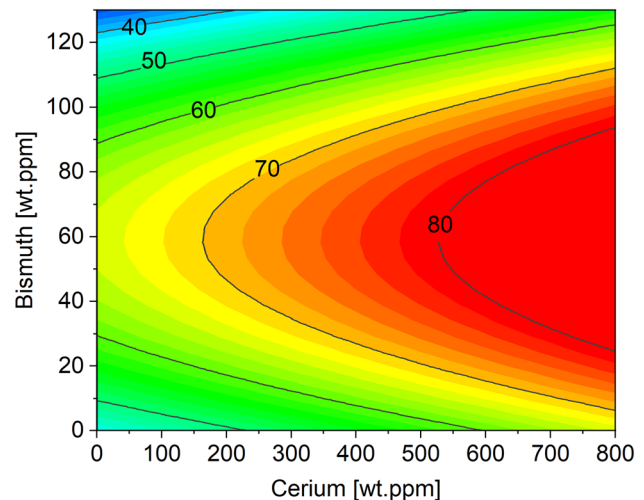


Figure 10. Modelled fraction of the graphite particles with form V on the total number of graphite particles depending on the amount of Ce and Bi.

Therefore, the occurrence of UG was not modelled either, as sample 11 is the single data point with UG remaining in the dataset.

The mathematical models do not claim to precisely represent the physical behaviour of the material system, but primarily serve to better visualise the experimental results. They can therefore only illustrate trends of the graphite morphology as a function of Ce and Bi content.

The influence of Bi and Ce on the nodularity is shown in Figure 8. Here, the proportions of graphite forms V and VI on the total graphite amount are shown in different colours depending on the contents of Bi and Ce, as they are considered to be nodular graphite. Figure 8 is therefore linked

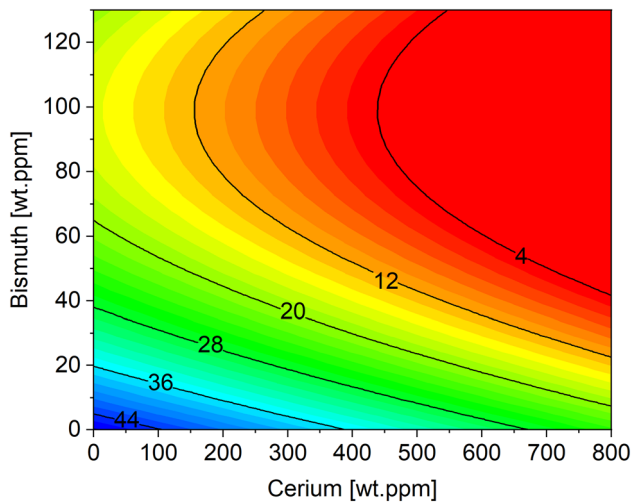


Figure 11. Modelled fraction of the graphite particles with form VI (smooth round nodules) on the total number of graphite particles depending on the amount of Ce and Bi present.

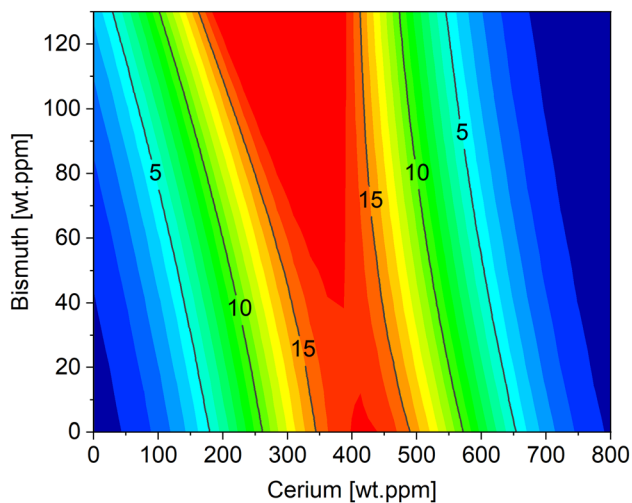


Figure 12. Modelled area fraction of chunky graphite on the total micrograph area.

to Figures 9, 10 and 11, which show the proportion of each single graphite form.

As shown in Figure 8, Bi begins to drastically lower the nodularity from around 60 starting at around 50 wt ppm. For the highest amounts of Bi investigated at around 120 wt ppm, the nodularity drops below 35. While the lowest effective concentration of Bi has some dependence on the Ce content, Ce itself has little influence on the nodularity at all levels of bismuth.

The nodularity decreasing for increasing Bi can be explained by the increased proportion of form III graphite

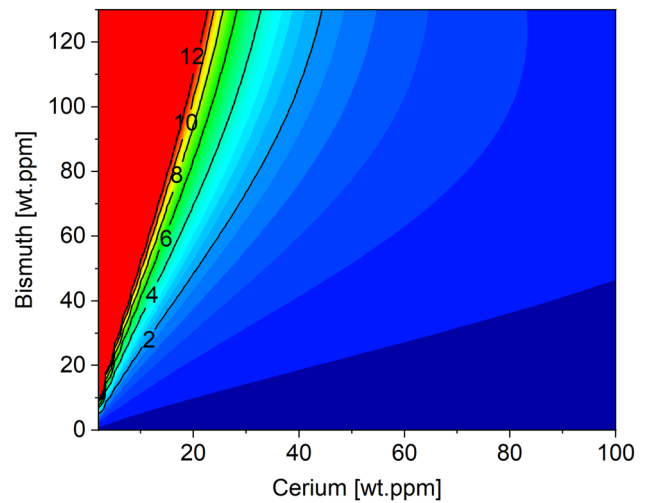


Figure 13. Modelled area fraction of intercellular lamellar graphite on the total micrograph area.

as displayed in Figure 9. A large excess of Ce relative to the Bi in turn can slightly lower the amount of form III graphite. For high concentrations of Bi and no Ce to counteract, form III ends up making up over half of all graphite.

Figure 10 shows the fraction of graphite form V on the total graphite, which is highly dependent on the level of Ce. For high Ce amounts, starting at around 500 wt ppm, up to 80% of graphite particles are classified as form V. A greater influence of Bi is observed, as compared to the effect of Ce on form III. As Bi content increases to values around 60 wt ppm, the amount of form V graphite initially increases for the same Ce content. With further increase to even higher Bi content of around 120 wt ppm, the fraction of form V decreases again.

Figure 11 shows the fraction of form VI graphite. As is shown, elevated concentrations of Ce and Bi both lead to a decrease in the optimal form VI graphite. They differ in that the graphite is transformed by Bi to form III and by Ce to form V, respectively, as shown in Figures 9 and 10. Combined addition of both elements results in an even greater reduction of the amount of form VI compared with their individual effects. The increasing fractions of form VI graphite at Bi contents higher than 100 wt ppm can be attributed to the higher amount of form VI graphite in sample 14 when compared with the neighbouring samples and are considered to be an outlier.

Besides the graphite morphology parameters, the occurrence and fraction of ILG and CHG were modelled as well. In Figure 12, the fraction of CHG on the total graphite is shown. For low concentrations of Ce, CHG could not be found. The fraction of CHG then increases to over 15% at 300 to 400 wt ppm Ce and decreases again above that until

no CHG appears around 700 wt ppm Ce. The incline of the CHG field towards lower Ce for higher Bi can be considered an artefact introduced by the exact composition of sample 8.

In Figure 13, the fraction of ILG is shown depending on the contents of Bi and Ce. It becomes clearly visible that even at low amounts of Bi ILG can be found in the microstructure. However, the addition of small amounts of Ce to the melt helps in avoiding the formation of ILG. A complete suppression of the formation of ILG can be achieved at a Ce content of about 50 wt ppm.

Discussion

The results show two key aspects, the ability of Ce and Bi to produce different forms of degenerated graphite and the influence they have on the graphite which is not degenerated. While certain critical concentrations could be observed for the precipitation of the degenerated graphite forms, we observed gradual changes of the share of each of the regular graphite forms III, V and VI with respect to the concentration of the interfering elements.

Bi is shown in Figure 9 to also produce graphite of form III irrespective of ILG formation. Thus, the content of Bi in a ductile iron melt should be as low as possible if at all necessary. The presence of ILG in the ductile iron microstructure, caused by the presence of Bi, can be effectively avoided by Ce addition as shown in Figure 13. However, by increasing additions of Ce to the melt the graphite growth tends to change from form VI to V (Figure 10), and it additionally provokes the growth of CHG (Figure 12) or UG. Therefore, only small amounts of Ce should be added to the melt to counteract interfering elements of the ILG provoking group, since its negative effects outweigh the prevention of ILG even at medium levels.

No samples investigated did show the formation of two different types of graphite degenerations simultaneously. CHG was formed for ratios Ce/Bi from 0.69 (sample 8) up to 15.4 (sample 23) or even 97.5 (sample 1), ILG appeared for Ce/Bi up to 1.5 (sample 20) and UG was found for a Ce/Bi ratio as low as 7.5 (sample 11). The absence of degenerations in samples 9, 10, 17, 21 and 24 cannot be explained neither by their Ce and Bi concentrations, nor by their Ce/Bi ratios as these are between the above values. The Ce/Bi ratios at which each degenerated graphite morphology occurred overlap. Hence, a precise prediction of the graphite morphology is not possible based on the concentrations of Ce or Bi, nor the ratio Ce/Bi.

CHG was found in cast iron samples with Ce contents ranging from 44 to 370 wt ppm. However, some samples in this concentration range did not exhibit any graphite

degeneration. It must be stressed that all samples with one Bi concentration were produced from one melt in the same mould, depicted in Figure 1a). Therefore, all parameters influencing the graphite morphology apart from the concentration of Ce were identical and all differences in microstructure observed can be attributed solely to the varying amounts of Ce.

Based on the formation of intermetallic compounds from CHG- and ILG-promoting elements, it could be assumed that if both are present in the melt, no growth of degenerate graphite should occur. At the stoichiometric ratios of the intermetallic compounds, no graphite degeneration would be expected. However, as shown in Figure 7, the material behaved differently in this investigation. Samples without degenerated graphite are found in between those with CHG with no apparent degeneration-free zone. In some samples with the same Bi concentration, CHG can be found at lower Ce concentrations, while even more Ce leads to the absence of degenerations. This is evident by comparing samples 8 (with CHG) against 9 and 10 (both without degeneration), 15 and 16 (both with CHG) against 17 (no degeneration) and 22 and 23 (both with CHG) against 24 (no degeneration). Interestingly, sample 21 shows no degeneration at the same Bi content even at lower Ce than sample 22; thus, at higher and lower Ce contents than those of samples 22 and 23 CHG did not occur.

CHG has been shown to grow early in the solidification,⁸ whereas UG formed in the LTF regions and hence, at the very end of solidification as shown by the etching in Figure 6. However, graphite with features of CHG also occurring in the LTF regions has been described previously.³⁶ The shape and size of those particles are very similar to early formed CHG in the same publication and match the CHG formed here as well. In comparison with the CHG, UG in this work formed mainly particles around 100 times smaller. UG and CHG can thus be distinguished by shape, Ce level necessary to their formation and location they are found in, which is equal to the time during solidification in which they precipitated. It is therefore likely that UG is formed by different formation mechanism in comparison with the CHG found at medium Ce levels.

Since no CHG was observed above Ce concentrations of 370 wt ppm, it can be assumed that higher concentrations prevent the formation of CHG under the exact conditions the samples were prepared. Since the distribution of samples without degenerated graphite did not show an apparent regularity, the limit of 370 wt ppm should be treated with caution. When alloying Ce at higher concentrations, the inevitable shift of the regular graphite from form VI to V must be considered, as well as the increased risk of UG formation, which was first observed at 594 wt ppm Ce.

If the porosity observed resulted from a diminished feeding capability as opposed to greater feeding need of alloys with

high Ce contents, this would fit with the formation of many tiny graphite particles in the LTF regions, which is how UG presented. Both could be explained by Ce reducing the number or the potential of available substrates for graphite nucleation, consistent with its high reactivity, exceeding even that of magnesium.³⁷

Ultimately, a concentration of Bi and Ce or ratio of both elements where the graphite in SSDI will not degenerate cannot be clearly specified. It is possible to counteract contamination with Bi, which would lead to ILG formation, by adding Ce. On the contrary, the addition of Bi to prevent CHG does not seem to be possible. However, these metallurgical measures are carried out at the expense of the regular spheroidal graphite and a predominant formation of regular form VI graphite cannot be achieved. Instead, further addition of either element to the melt results in the decrease in form VI and an increase in graphite forms III and V till they make up the entirety of graphite particles.

Summary

- High additions of Ce to the melt significantly increased the porosity of SSDIs.
- Intercellular lamellar graphite was found for low contents of 25 wt ppm Bi, up to 37 wt ppm Ce and Ce/Bi up to 1.5.
- Chunky graphite was found in samples with Ce contents as low as 44 wt ppm and up to 370 wt ppm with ratios of Ce/Bi between 0.69 and 15.4.
- Undercooled graphite was present in samples with cerium levels upward of 594 wt ppm and was the only degenerated morphology present above 1000 wt ppm of Ce.
- Except for chunky graphite and exploded graphite, no two kinds of degenerated graphite were present in the same sample together.
- Graphite degenerations by Bi could be avoided using Ce.
- Graphite degenerations by Ce could be avoided in some samples, but an underlying mechanism could not be found.
- While Ce and Bi will counteract the formation of graphite degenerations from the other element respectively in some samples, a distinct ratio Ce/Bi that prevented graphite degenerations could not be determined.
- Bismuth causes a large increase in the amount of form III graphite, which is independent of its ability to form intercellular lamellar graphite and even persists if the intercellular lamellar graphite was avoided by Ce addition.
- Cerium causes a large increase in the amount of form V graphite at the expense of form VI even at compositions where CHG did not form.

- For high levels of Ce and Bi, the entirety of graphite will be present as degenerations, forms III and V graphite, whereas form VI graphite disappears.

Author Contributions FS conceived and designed the analysis, collected the data, performed the analysis and wrote the paper. DF collected the data and performed the analysis. BT conceived and designed the analysis and wrote the paper.

Funding

Open Access funding enabled and organized by Projekt DEAL. Research was funded by Clausthal University of Technology.

Data Availability

Data are available on request from Felix Stieler and Babette Tonn.

Conflict of interest The authors declare that they have no conflict of interest.

Open Access

This article is licensed under a Creative Commons Attribution 4.0 International License, which permits use, sharing, adaptation, distribution and reproduction in any medium or format, as long as you give appropriate credit to the original author(s) and the source, provide a link to the Creative Commons licence, and indicate if changes were made. The images or other third party material in this article are included in the article's Creative Commons licence, unless indicated otherwise in a credit line to the material. If material is not included in the article's Creative Commons licence and your intended use is not permitted by statutory regulation or exceeds the permitted use, you will need to obtain permission directly from the copyright holder. To view a copy of this licence, visit <http://creativecommons.org/licenses/by/4.0/>.

REFERENCES

1. H. Löblich, W. Stets, *Giesserei* **100**, 30 (2013)
2. H. Werner, I. Lappat, B. Aurich, *Giesserei* **103**, 38 (2016)
3. J. Sertucha, J. Lacaze, J. Serrallach, R. Suárez, F. Osuna, *Mater. Sci. Technol.* **28**, 184 (2012). <https://doi.org/10.1179/1743284711Y.0000000014>
4. International Organization for Standardization, *Microstructure of cast irons—part 1, Graphite classification by visual analysis (ISO 945-1:2019)* 77.080.10(ISO 945-1:2019), Geneva, Switzerland.
5. International Organization for Standardization, *Microstructure of cast irons—part 2: graphite*

- classification by image analysis (ISO 945-2:2011) 77.080.10(ISO 945-2:2011), Geneva, Switzerland.
6. W. Maschke, *Giesserei*, **36** (2015)
 7. J. Lacaze, L. Magnusson Åberg, J. Sertucha, in *Keith Mills [i.e. Millis] Symposium on Ductile Cast Iron 2013* (Curran, Red Hook, 2014), pp. 360–368
 8. B. Tonn, J. Lacaze, S. Duwe, *Mater. Sci. Forum* **925**, 62 (2018). <https://doi.org/10.4028/www.scientific.net/MSF.925.62>
 9. L. Dekker, B. Tonn, G. Lilienkamp, *Int. J. Metalcast.* **14**, 827 (2020). <https://doi.org/10.1007/s40962-020-00434-1>
 10. R.K. Buhr, *AFS Trans.* **79**, 247 (1971)
 11. E.N. Pan, C.-Y. Chen, *AFS Trans.* **104**, 845 (1996)
 12. J. Lacaze, D. Connétable, M.J. Castro-Román, *Materialia* **8**, 100471 (2019). <https://doi.org/10.1016/j.mtla.2019.100471>
 13. Z.H. Li, Y.X. Li, *Mater. Sci. Forum* **475–479**, 2769 (2005). <https://doi.org/10.4028/www.scientific.net/MSF.475-479.2769>
 14. B. Prinz, K.J. Reifferscheid, T. Schulze, R. Döpp, E. Schürmann, *Giessereiforschung* **43**, 107 (1991)
 15. A. Javaid, C.R. Loper Jr., *AFS Trans.* **103**, 135 (1995)
 16. P. Larrañaga, I. Asenjo, J. Sertucha, R. Suarez, I. Ferrer, J. Lacaze, *Metall. Mater. Trans. A* **40**, 654 (2009). <https://doi.org/10.1007/s11661-008-9731-y>
 17. H. Nakae, M. Fukami, T. Kitazawa, Y. Zou, *China Foundry* **8**, 96 (2011)
 18. Y. Kato, Y. Zou, H. Nakae, *Key Eng. Mater.* **457**, 37 (2010). <https://doi.org/10.4028/www.scientific.net/KEM.457.37>
 19. H. Nakae, S. Jung, H.-C. Shin, *J. Mater. Sci. Technol.* **24**, 289 (2008)
 20. U. de La Torre, J. Lacaze, J. Sertucha, *Int. J. Mater. Res.* **107**, 1041 (2016). <https://doi.org/10.3139/146.111434>
 21. T. Thielemann, *Giessereitechnik* **16**, 16 (1970)
 22. M.V. Mozharov, A.M. Petrichenko, N.P. Zhabotinskii, S.I. Serkhovets, *Izvestiya Vysshikh Uchebnykh Zavedenij. Chernaya Metallurgiya* **119** (1976)
 23. R. González-Martínez, U. de La Torre, J. Lacaze, J. Sertucha, *Mater. Sci. Eng. A* **712**, 794 (2018). <https://doi.org/10.1016/j.msea.2017.11.050>
 24. J. Sertucha, J. Lacaze, S. Armendariz, P. Larrañaga, *Metall. Mater. Trans. A* **44**, 1159 (2013). <https://doi.org/10.1007/s11661-012-1592-8>
 25. J. Sertucha, J. Lacaze, R. González-Martínez, *IOP Conf. Ser. Mater. Sci. Eng.* **529**, 12017 (2019). <https://doi.org/10.1088/1757-899X/529/1/012017>
 26. W. Baer, *Int. J. Metalcast.* **93**, 28 (2019). <https://doi.org/10.1007/s40962-019-00363-8>
 27. L. Magnusson Åberg, C. Hartung, J. Lacaze, in *10th International Symposium on the Science and Processing of Cast Iron Proceedings*, ed. by R. Boeri, J.M. Massone, G. Rivera (2014)
 28. B. Bauer, I. Mihalic Pokopec, M. Petrič, P. Mrvar, *Int. J. Metalcast.* **14**, 1052 (2020). <https://doi.org/10.1007/s40962-020-00419-0>
 29. Z. Glavas, A. Strkalj, K. Maldini, F. Kozina, *Arch. Metall. Mater.* **63**, 1547 (2018). <https://doi.org/10.24425/123846>
 30. P. Ferro, A. Fabrizi, R. Cervo, C. Carollo, *J. Mater. Process. Technol.* **213**, 1601 (2013). <https://doi.org/10.1016/j.jmatprotec.2013.03.012>
 31. H. Morrogh, *AFS Trans.* **60**, 439 (1952)
 32. M.N. Abdusalyamova, A.G. Chuiko, E.I. Shishkin, O.I. Rachmatov, *J. Alloys Compd.* **240**, 272 (1996). [https://doi.org/10.1016/0925-8388\(96\)02314-6](https://doi.org/10.1016/0925-8388(96)02314-6)
 33. T.B. Massalski, H. Okamoto, *Binary Alloy Phase Diagrams* (ASM International, Materials Park, 1990)
 34. International Organization for Standardization, *Spheroidal Graphite Cast Iron—Classification* (ISO 1083:2018) 77.080.10(ISO 1083:2018), Geneva, Switzerland.
 35. International Organization for Standardization, *Microstructure of cast irons—part 4: test method for evaluating nodularity in spheroidal graphite cast irons* (ISO 945-4:2019) 77.080.10(ISO 945-4:2019), Geneva, Switzerland
 36. Tang Chong Xi, J. Fargues, M. Hecht, J.C. Margerie, *Fonderie-Fondeur d’Aujourd’hui*, 14 (1985).
 37. I. Barin, O. Knacke, O. Kubaschewski, *Thermochemical Properties of Inorganic Substances* (Springer, Berlin, 1977)

Publisher’s Note Springer Nature remains neutral with regard to jurisdictional claims in published maps and institutional affiliations.